# Tuning band alignment at grain boundaries for efficiency enhancement in CZTS solar cells

Wenjie Li<sup>1\*</sup>, Weimin Li<sup>†1</sup>, Guo Chen<sup>1</sup>, Liyun Wu<sup>1</sup>, Jun Zhang<sup>2</sup>, Ming Chen<sup>1</sup>, Guohua Zhong<sup>1</sup>,

Junyi Zhu<sup>3</sup>, Ye Feng<sup>1\*</sup>, Hao Zeng<sup>4\*</sup>, Chunlei Yang<sup>1\*</sup>

<sup>1</sup>Shenzhen Institute of Advanced Technology, Chinese Academy of Science, Shenzhen, China <sup>2</sup>School of Physical Science and Technology, Lingnan Normal University, Zhanjiang, China <sup>3</sup>Department of Physics, The Chinese University of Hong Kong, Shatin, Hong Kong, China <sup>4</sup>Department of Physics, University at Buffalo, the State University of New York, Buffalo, NY, USA

#### **Abstract**

Conducting atomic force microscopy has been performed for the fundamental understanding of the mechanism responsible for the lower power conversion efficiency (PCE) of CuZnSnS<sub>4</sub> (CZTS) solar cells than that of CuIn<sub>1-x</sub>Ga<sub>x</sub>Se<sub>2</sub> (CIGS) solar cells. The difference in efficiency is partly attributed to the distinctly different band alignment between the grain boundaries (GBs) and grain interior (GI) for the two materials. While CIGS shows type-II band alignment, CZTS was discovered to demonstrate type-I band alignment with the conduction band shifting downward while the valence band shifting upward at the GBs. The type-I band alignment in CZTS leads to both electron and hole trapping enhancing their recombination and lowers the PEC. Band engineering was realized by moderate oxidative annealing of CZTS. The preferential GB oxidation changes the band alignment into inverse type-I (*i.e.* the conduction band upward bending and Valence Band downward bending at GBs). The blocking of carrier recombination at GBs leads to 30% enhancement in PCE. Our work reveals the critical role of band alignment between the grain boundary and interior plays in polycrystalline thin film solar cells, and suggests band alignment

engineering as a practical approach to enhance PCE. Furthermore, conducting AFM has been shown to be a powerful tool for qualitative and semi-quantitative characterization of band alignment in polycrystalline films.

#### 1. Introduction

CuIn<sub>1-x</sub>Ga<sub>x</sub>Se<sub>2</sub> (CIGS) is one of the most successful light absorber materials for thin film solar cells. CIGS solar cells hold the current world record of efficiency with the value of 23.35% among all stable, inorganic polycrystalline thin film solar cells and have attracted considerable interest in both academia and industry. However, the rare elements In and Ga in CIGS are costly, which hindered their large scale production. With In and Ga in CIGS absorber substituted by earth abundant and low-cost Zn and Sn, kesterite Cu<sub>2</sub>ZnSnS<sub>4</sub> (CZTS) is regarded as one of the promising alternatives for CIGS and have received significant attention in recent years [1-10].

Although possessing similar structures, optical and electrical properties with CIGS, the highest PCE achieved thus far for CZTS and Cu<sub>2</sub>ZnSn(S,Se)<sub>4</sub> (CZTSSe) solar cells are 9.2% [3] and 13.0% [4], respectively, both are much lower than the 23.35% record for CIGS solar cells [11]. This is caused partly by the significant open circuit voltage (V<sub>oc</sub>) deficit in these devices [6]. The minority-carrier lifetime of kesterite is a few nanoseconds as shown by photoluminescence characterization [12], which is much shorter than the 250 ns for the lifetime of CIGS [13]. This indicates the presence of strong recombination of photogenerated carriers in CZTS films. Many studies suggested that the deep energy level defects in the bulk such as Zn<sub>Cu</sub> anti-sites and Sn related defects are responsible for the carrier recombination. This assumption is followed by many studies both theoretically and experimentally [14-17], while the role of grain boundaries (GBs) remains controversial[10,18,19].

Typically, semiconductor materials for photovoltaic applications perform worse in their polycrystalline phase due to the presence of defects at GBs that act as recombination centers. However, in the case of polycrystalline CIGS, a remarkable photovoltaic performance better than its single crystalline counterpart has been achieved, suggesting the benign grain boundaries. Zunger *et al.* suggested a hole barrier at GBs, which was confirmed by a direct band alignment measurement of CIGS at GBs *via* scanning tunneling microscopy [20]. A type-II band alignment between GB and grain interior (GI) was found, where the valance and the conduction

bands of the GB has higher energy than that of the GI with a downward offset for both the conduction and valence bands. The downward valence band offset at GBs leads to a hole depletion region, which makes the GB a hole transport barrier; on the other hand, the downward conduction band offset drives the electrons to the GBs. This type-II band alignment at GBs serves two purposes: it suppresses electron-hole recombination, and provides a pathway for minority carrier transport [21-24].

In the case of CZTS, Clemens et al. suggested a beneficial role of the GBs with enhanced photocurrents [10]. Polizzotti et al. proposed that the copper-poor ordered defect complex (ODC) model may apply to CZTSSe GBs in a similar fashion to that for CIGS [25]. However, energy dispersive x-ray spectroscopy (EDS) analysis of CZTS films demonstrates that GBs appear to have either the same composition as the GIs or are Cu rich [26]. Density-functional theory (DFT) calculation shows that constituent atoms at GBs in CZTSSe and CZTS created localized defect states that promote the recombination of photo-generated carriers [27-29]. These conflicting results suggest that the mechanism responsible for the lower efficiency of CZTS (CZTSSe) remains elusive [7, 8], despite extensive research in the past. As benign grain boundaries are essential for reaching high efficiency in CIGS solar cells, elucidating the role of GBs in CZTS is crucial for enlightening the underlying mechanism responsible for the low efficiency of CZTS solar cells, and may guide device optimization to improve the efficiency.

In this work, conducting atomic force microscopy (C-AFM) with the capability of nm-scale electrical characterization has been applied to study the band alignment at GB of the absorber films in thin film solar cells. A metal probe (Pt) was brought into contact with the semiconductor surface under Ar atmosphere (H<sub>2</sub>O and O<sub>2</sub> < 1 ppm) to avoid current induced chemical changes. With good Schottky contact between the metal tip and oxide-free surface of the semiconductor, The Pt AFM tip can work as a top electrode to collect the photocurrent generated at the absorber. Thus, the local electrical and photovoltaic performance can be measured, and the conduction and valance band offsets between GB and neighboring GI can be obtained. Moreover, the Schottky barrier height from voltage-current measurements was used to extract the

valence band offset at GBs. This allowed a fast and reliable measurement of band alignment at GBs in CZTS.

The conduction and valance band offsets at GBs for both CIGS and CZTS films have been studied. An upward valance band offset was observed in CZTS, which is opposite to the case of CIGS. These results indicate the existence of hole traps rather than hole barriers at the GBs for CZTS, resulting in enhanced carrier recombination at GBs for photon-generated carriers.

To mitigate the detrimental effect of GBs of CZTS, we further engineered the band structure at GBs by moderate oxidative annealing. Such annealing reverses the band offset at GBs, turning it from type-I to inverse type-I, i.e. the valence band turned from upward bending to downward bending, while the conduction band changed from downward to upward bending. This changes the role of GBs from recombination centers into barriers for charge transport, and improves the photovoltaic performance significantly. Our work not only elucidates the critical role of electronic structures at grain boundaries, but also provides an effective approach for improving the efficiency of thin film solar cells. Meanwhile, conducting AFM has been used for the first time to qualitatively and semi-quantitatively determine the band alignment at the GBs in polycrystalline films.

### 2. Experimental

For CIGS samples studied, 1.7  $\mu$ m thick Cu<sub>0.9</sub>In<sub>0.7</sub>Ga<sub>0.3</sub>Se<sub>2</sub> films were grown on Mo-coated soda-lime glass via a three-stage co-evaporation process, as described elsewhere [30]. Cells with > 18% efficiency were obtained with this type of films. The final composition is Cu-poor ([Cu]/([In]+[Ga])=0.9) as determined by x-ray fluorescence measurements. For CZTS samples, 1.4 $\mu$ m thick CZTS films were deposited on Mo-coated soda-lime glass using co-sputtering of Cu, ZnS and SnS<sub>2</sub> targets in 2% H<sub>2</sub>S/Ar mixture atmosphere. Then the films were annealed at 535°C in 6.4% H<sub>2</sub>S/N<sub>2</sub> atmosphere as described elsewhere [31]. The final composition of the film is Cu-poor ([Cu]/([Zn]+[Sn])=0.9) as determined by x-ray fluorescence

measurements.

After the preparation, the film samples were transferred to a glove box under argon atmosphere (O<sub>2</sub> and moisture content less than 1 ppm) immediately for CP-AFM measurements. To remove the surface oxide during the transfer, a standard chemical etching was carried out in the glove box. The CIGS samples were first etched in Br<sub>2</sub>/methanol, followed by etching in KCN/H<sub>2</sub>O solution (0.1 M) for 2 min. After etching, the samples were rinsed in deionized water followed by methanol. CP-AFM measurements were performed using a CSPM5500 system (Being, China) with all-metal Pt AFM probes (RMN-25PT400B, 8 N/m, Rocky Mountain Nanotechnology) in contact mode. Fig. 1(a) shows the schematic diagram of the experimental setup. In the CP-AFM measurements, the Pt tip was brought into contact with the freshly cleaned p-type CIGS or CZTS layer, forming a Schottky contact, as confirmed by the rectifying I-V curves measured. The Schottky barrier height depends on the difference between the energy of the valence band maximum (VBM) of the semiconductor and the Fermi level of the Pt probe, as shown in Fig. 1(b). Similar to the p-n junction formed in the completed solar cells, a depletion region is formed at the Pt/absorber Schottky junction and the photogenerated electrons and holes are separated in the depletion region and the electrons are collected by the Pt AFM tip as the top electrode. Current mapping can be obtained by collecting the local current at a given tip bias during the topography scan at nanoscale spatial resolution. Illuminating the CZTS surface by an external laser (650 nm) at an intensity of 100 mW/cm<sup>2</sup> further allows the probing of local photocurrent and photovoltaic performance. Current mapping in dark condition was measurement by CP-AFM at dark-lift mode. The laser was turned off when measuring the current, so the laser will not affect the measurement.

GB treatment was carried out *via* annealing the samples in a chamber filled with air, saturated water vapor and dry air (O<sub>2</sub>+N<sub>2</sub>), respectively. After the CZTS films samples were prepared, they were exposed to the environment at 200 °C for 5 min before being taken out of the chamber. The samples were then etched in a KMnO<sub>4</sub>/H<sub>2</sub>O solution (0.0005 M) for 10 s and rinsed in deionized water, followed by

etching in KCN/H<sub>2</sub>O solution (0.1 M) for 5 min in the glove box to remove surface oxides. After etching, the samples were first rinsed in deionized water, then methanol and finally dried with argon stream. CZTS solar cells cells were prepared with this type of films.

For TEM and EDS measurements, a Philips Tecnai F20 microscope equipped with an Oxford EDS detector was used. To obtain the composition mapping at GBs with nm spatial resolution, EDS measurements were performed in STEM mode with drift correction. The sample orientation was adjusted so that the grain boundary was nearly parallel to the electron beam as described previously [23].

To further characterize the valance band alignment at GBs, dark I-V curves were measured. As is well known, in the dark condition, the relationship between I and V follows the below equation:

$$I = I_s(exp(V/nkT) - 1)$$
 (1),

where  $I_s$  is the saturation current and n is the ideality of the Schottky junction. For V > 50 mV, the -1 term can be neglected, and taking logarithm for both sides gives:

$$lnI = lnI_s + V/nkT (2).$$

When plotting the lnI against the voltage, the slope gives 1/nkT and the intercept gives  $ln(I_s)$ . Meanwhile  $I_s$  can be described by the equation:

$$I_s = A^*AT^2 exp(-q\Phi/nkT)$$
 (3),

where  $A^*$  is the Richardson constant, A is the area of the contact and  $\Phi$  is the Schottky barrier height. Taking logarithm for both sides gives:

$$lnI_{S} = lnA^{*} + lnA + lnT^{2} - q\Phi/nkT$$
 (4).

Combing all the equations described above, we can relate the intercept of the linear fit of the logarithm I-V curves to the Schottky barrier height  $\Phi$ . Since the Schottky barrier height is caused by the energy difference between the valence band edge of the absorber and the Fermi level of the metal probe, the barrier height value depends monotonically on the valence band energy level, if not completely determined due to the pinning effects. A smaller  $\ln I_s$  corresponds to a higher Schottky barrier and a lower valence band edge level.

#### 3. Results and Discussions

## 3.1 Downward conduction band bending at GBs vs. GIs measured by photocurrent

To study the band alignment at GBs, two types of thin film samples including CIGS and CZTS were investigated using CP-AFM. The topographic images of the CIGS and CZTS thin films are shown in Fig. 2a-b, along with the corresponding photocurrent mapping (Fig. 2c-d). The photocurrent images were taken at zero bias under 100 mw/cm<sup>2</sup> illumination. The following features have been observed for both CIGS and CZTS thin films: Firstly, grains with sizes of micrometers can be clearly identified in the topography. Similar to our previous result measured in a UHV system [23], continuous and stable photocurrent appearing at all measured area indicates that the CIGS and CZTS surface is clean and oxide free, which is crucial for our CP-AFM measurements. Secondly, a much larger photocurrent appears at GBs for both samples compared to that at GIs, as evidenced by the brighter contrast at GBs. Since the photocurrent at Zero bias is determined by the rate of electrons flowing from the conduction band to the AFM tip, the larger photocurrent at GBs suggests that more photogenerated electrons accumulate at GBs. It manifests that the energy of the conduction band minimum (CBM) at GBs is lower than that at GIs. Such band offset near GBs drives the photo-excited electrons to flow towards the GBs [23, 32]. The larger photocurrent at GBs is more evident when comparing Fig. 2(e) to 2(f), which compares the I-V curves under light illumination measured at positions marked as GB and GI (shown in Fig. 2(c) and 2(d)). Meanwhile it's noticeable that the brighter contrast area at GBs of the CZTS photo current mapping is narrower than that of CIGS photo current mapping as shown in Fig. 2(c) and(d). This result manifests narrower GBs of CZTS films.

# 3.2 Opposite valence band bending at GBs vs. GIs for CIGS and CZTS measured by tunneling current

To obtain band alignment information on the valence bands, we carried out tunneling current mapping by dark I-V measurements (see experimental section for more details) for CIGS and CZTS. The behaviors of the GBs between CIGS and CZTS show clear contrast, as seen from Fig.3 (a) and Fig. 3(b). Dark boundaries are observed in CIGS, while bright boundaries are found in CZTS. These results suggest that the dark current at GBs is lower than that at GIs for CIGS, while vice versa for CZTS. This is further confirmed by showing the tunneling I-V curves at selected positions around GBs with opposite behaviors for CIGS and CZTS, as seen from Fig. 3(c) and 3(d). The insets in Fig. 3(c) and Fig. 3(d) show the linear fitting of the I-V curves in the logarithmic scale. A typical rectifying I-V characteristics is observed, indicating a Schottky contact between the metal tip and the CIGS (CZTS) surface. The intercept of the I-V curve fitting with the y-axis gives the height of the Schottky barrier. For CIGS, the turn-on voltage of the I-V curve at GB is larger than that at GI. This suggests that the valence band at GB shifts downward relative to that at GI. While for CZTS, the turn-on voltage at GBs is clearly smaller than that at GIs. This indicates that the Schottky barrier height is larger at GI. A smaller Schottky barrier height at GBs reveals an upward valence band bending around GBs than at GIs in CZTS. Meanwhile, narrower contrast area at GBs from photo current mapping are observed for CZTS than that of CIGS films as shown in Fig. 3(a) and(b). This result is consistent with the observation in Fig.2 indicating narrower GBs in CZTS films.

#### 3.3 Proposed band alignment for CIGS and CZTS around GBs

Combining the above results and analyses, we can draw the schematic band alignment diagram for CIGS and CZTS samples, as shown in Fig. 4(a) and 4(b), respectively. For CIGS, both conduction band and valance band show downward band bending at GBs, leading to a type-II band alignment. This is mainly caused by an ODC layer formed at GBs [21]. This type of band alignment can enhance the separation of the photogenerated electrons and holes. Electrons are accumulated while holes are depleted at GBs, *i.e.* the GBs serve as electron conduction channels while being barriers for hole. This result is consistent with previous experimental observations in literatures revealing the benign behavior of the GBs in CIGS [20][23]. The CP-AFM results for CIGS are in a good agreement with our previous STS data, which indicate that this method is reliable and can qualitatively identify the band

alignment of polycrystalline thin films around GBs. This result is also consistent with the downward band bending at GBs from SKPM measurement in the literature [21]. But SKPM measurement can only measure surface potential variation at GBs, which is only one of the possible reasons which can cause band bending at GBs. In our work, the band bending for both conduction band and valence band were measured from the current mapping differences at GBs directly driven by the band offsets. So it can characterize the band bending not only from the surface potential but also others possible causes such as defect structure at GBs itself.

For CZTS, downward conduction band bending and upward valance band bending is observed, leading to a type-I band alignment at GBs. This type of band alignment leads to confinement of both electrons and holes at GBs, which enhances their recombination. This is likely one of the major causes for the lower PCE of the CZTS solar cells.

Correlation between the band alignment and the local device performance was studied to understand the effect of band alignment at GBs. Local photovoltaic performance at the same GBs was characterized by current mapping under positive and negative bias. Fig. S1(a), (b) and (c) shows the topography and simultaneous current images of a CZTS sample taken with a tip bias of +1 and -1 V under the dark condition, respectively. In Fig. S1(b), higher currents were observed at all GBs when scanned at a tip bias of +1 V, corresponding to a lower current threshold in the rectifying I-V curves, which is consistent with the result shown in Fig. 3(d). Higher current areas in the current image clearly overlap with the GBs, further confirming that a smaller Schottky barrier height caused by the valence band upward bending is a general behavior of GBs.

Higher currents at GBs were also observed when scanned at a tip bias of -1 V under the dark condition as shown in Fig. S1(c), indicating a large leakage current at GBs. This is further depicted by the local dark I-V curves measured at neighboring GB and GI as shown in Fig. S1(d), with a magnified scale for negative bias scan. Large leakage current is directly responsible for the local lower shunt resistance and fill factor and could be possibly related to higher electron and hole recombination at

GBs in CZTS. The lower shunt resistance at GBs will adversely affect the overall photovoltaic performance of the CZTS solar cells.

Furthermore, the EDS analysis was performed in the drift corrected STEM mode and the results are shown in Fig.S2 (a) and (b). A GB perpendicular to the film surface was confirmed by selected area diffraction (SAD). Only one set of SAD pattern was observed in the grain adjacent to the GB. Along the chosen line as marked in the TEM image of Figure S2 (a) across a grain boundary, no appreciable difference of the concentrations of Cu, Zn, Sn and S was observed between GB and adjacent GI regions, as depicted in Figure S2 (b), suggesting no ODC layer at GBs in CZTS, as opposed to the situation in CIGS. The reason for the type-I band alignment remains unclear, and detailed atomistic structural probes together with first principles calculations are needed to elucidate the mechanism.

#### 3. 4 Engineering the band structure of the GBs in CZTS via air annealing

## 3.4.1 Photocurrent and tunneling current characteristics for CZTS after air annealing

From the above experiments, it can be concluded that the detrimental GBs is one of the major issues responsible for the efficiency loss for CZTS solar cells. Therefore, it is expected that engineering the electronic structure of the GBs may enhance the performance of the CZTS solar cells. It has been shown earlier that low temperature air annealing is an effective way to improve performance. One possible reason for the increased efficiency of the CZTS solar cells is the oxides formed at GBs during the air annealing.

Fig. 5(a) and Fig. 5(b) show the photocurrent and tunneling current mapping of CZTS after the annealing process (see Experimental section for details). Instead of photocurrent enhancement at all GBs in pristine CZTS, dark boundaries (low current) were observed in both photocurrent and tunneling (dark) current images, indicating that carriers are blocked outside the GBs in the CZTS absorber. Fig.5 (c) depicts the I-V curves measured under light illumination at selected positions marked as GB and GI shown in Fig. 5(a). The I-V curves taken at GIs are very similar to the I-V curves

from CZTS before the oxidization treatment, while the I-V curves taken from GBs show negligible photocurrent. The blocked current around GBs suggests that there is a large upward conduction band bending around GBs compared to GIs. Fig. 5(d) shows the I-V curves at the same GB and GI under dark condition. The inset in Fig. 5(d) shows the linear fittings of the I-V curves in logarithmic scale. Different from the dark I-V curves from CZTS before the treatment, the intercept from the I-V curves at GBs is larger than that at GIs, indicating a larger Schottky barrier and a lower valance band edge at GBs. This result demonstrates that there is a downward valence band bending at GB after the oxidization treatment.

### 3.4.2 Proposed band alignment of CZTS around GBs before and after oxidative annealing

Based on the above results, we can draw the band alignment diagram for CZTS before and after the annealing process, as shown in Fig. 6(a) and (b), respectively. The band alignment for both conduction band and valence band has been modified by the annealing treatment. A downward bending of the conduction band has been changed into upward bending in CZTS after treatment, which repels photogenerated electrons from the GBs and causes greatly diminished photocurrent at GBs. Furthermore, an upward valence band bending has been changed into downward bending to turn GBs into a hole barrier, leading to a hole depletion region just as in the case of CIGS. This band alignment could cause depletion regions for both electrons and holes at GBs and greatly reduces electron and hole recombination at GBs in CZTS. The change in band alignment suggests that oxidative annealing effectively passivates the detrimental GBs, which can lead to improved photovoltaic performance for CZTS solar cells.

To further understand the treatment effects, EDS elemental analysis was performed in the drift corrected STEM mode on CZTS films to compare the composition at GBs and GIs. As described before, a perpendicular GB was selected and an EDS line profile was performed across the GB. Similar to the previous results on the untreated CZTS sample, no appreciable difference of the concentrations of Cu, Zn, Sn, S and O was observed between GB and adjacent GI regions. While in spot EDS spectrum measured with long acquisition time (60 seconds) a weak O peak

appeared at the GB as shown in Fig. S4 indicating a very thin oxide layer at GBs after annealing in air. The partial S vacancy could possibly be passivated by O and causes an upward conduction band bending and downward valance band bending at GBs and a larger band gap.

To examine the effect of the band alignment engineering further, microscopic device characterizations have been performed for the CZTS thin films after the annealing treatment. Fig. S5(a), (b) and (c) show the topography and simultaneously current images of a CZTS film sample taken at a tip bias of +1 and -1 V under the dark condition, respectively. In Fig. S5(b), lower currents are observed at all GBs when scanned at a tip bias of +1 V, indicating a higher current threshold in the rectifying I-V curves. This result illustrates a downward valence band bending at all GBs after the treatment. Fig. S5(c) shows the dark current mapping of CZTS after treatment when scanned at a tip bias of -1 V. Clearly, a much-reduced leakage current is observed at GBs in contrast to the case of the CZTS sample before the treatment. Fig. S5(d) shows a typical dark I-V curve measured at a neighboring GB and GI marked in Fig. S5(a), (b) and (c) with magnified scale for the negative bias scan. A lower current at a tip bias of +1 V for I-V curve at GB is observed which is consist with the result shown in Fig.S5(b). A smaller leakage current is observed in the rectifying I-V curves which confirmed the decrease of the leakage current at GBs due to the treatment. This result clearly demonstrates that a downward valence band bending leads to a higher shunt resistance at GBs which could lead to diminished electron and hole recombination.

Full solar cell devices were fabricated from the same batch of CZTS films with and without the air annealing treatment. The CZTS solar cells with treatment show significant improvements for both the open circuit voltage, from 620 mV to 672 mV and fill factor, from 53% to 65%. As a result, the cell efficiency is improved significantly from 6.2% to 8.1%, a 30% boost. As shown in Fig. S6, obvious increases of the fill factor ,  $V_{oc}$  were observed after the grain boundary treatment. This result clearly demonstrates the detrimental role the grain boundaries played for pristine CZTS solar cells. The type-I band alignment of CZTS solar cells can lead an

enhanced recombination of photo generated electrons and holes and cause lower fill factor and  $V_{oc}$  and thus the efficiency of the solar cells. This is further approved by the larger leakage current at grain boundaries of CZTS solar cells as shown in Figure S1. The direct correspondence between the microscopic band alignment engineering at GBs and overall device photovoltaic performance demonstrates the critical role of the band alignment at GBs for the photovoltaic performance of the CZTS solar cells.

From the above discussions, one can conclude that for CZTS after the annealing treatment, the downward valence band bending and upward conduction band bending cause both electron and hole depletion, which reduce the recombination at GBs. Further enhancement in performance by moderate air annealing, however, is limited by competing detrimental effects from the oxidized GBs. This is because the upward bending of the conduction band repels the photogenerated electrons from the GBs, unlike the GBs in CIGS serving as electron channels. Instead, the GBs in CZTS after the annealing treatment are transport barriers for both electrons and holes. A thicker oxidized GB means a larger volume fraction of inactive regions, which will in turn reduce the photovoltaic performance. We suggest that future work on band engineering to enhance the photovoltaic performance of the CZTS solar cells should focus on achieving a downward bending of the conduction band at GBs, e.g. by elemental substitution at GBs.

#### 3.4.3 Which is more effective in GB passivation: O<sub>2</sub> or water?

All annealing experiments performed up to now are processed in air which contains both O<sub>2</sub> and H<sub>2</sub>O. While a thin oxide layer was observed in GBs after annealing, the roles of O<sub>2</sub> and H<sub>2</sub>O is not clear at this stage. To investigate this aspect, we tested CZTS films with different treatments, namely annealing in dry air (O<sub>2</sub>+N<sub>2</sub>) and annealing in saturated water vapor (H<sub>2</sub>O+N<sub>2</sub>). The cross-sectional CP-AFM measurements of the samples were performed to study the effect of treatments on GBs in the film interior, as shown in the Schematic diagram of the experimental setup in Fig 7(a). After the treatments, the samples were cleaved in the glove box to avoid further oxidation and contamination of the fresh surfaces of the cross-sections before

the measurements. The tunneling current mappings under +1 V bias of the cross-sections of the CZTS thin films before and after air annealing are shown in Fig. 7(b-d). For CZTS without treatment, bright boundaries were observed in the cross section mapping, as shown in Fig 7b. The results appear similar to the current mapping of the surface of CZTS with no treatment (shown in Fig 3b). The band alignments, for the first time, were measured at the GBs in the interior of the CZTS film. The nearly identical results between the plain view surface and cross-section mappings proved the reliability of our measurements. This clearly demonstrates that the upward valance band bending at the GBs is intrinsic and not from artifacts. Comparing samples treated with dry air and water vapor, clear differences were observed. After treated with dry air, some GBs turn dark while some bright GBs remain intact, as shown in Fig 7c. The dark GBs in the current mapping suggest that the upward valance band bending at GBs has been partially changed into downward band bending. While for CZTS samples treated in saturated water vapor, all GBs turned dark, as shown in Fig. 7d. It shows that the passivation of the GBs by water vapor is more effective than by dry air. This result demonstrates that water vapor is more effective in passivating the GBs of CZTS. Recently, Sun et. al show that the post annealing in the moisture atmosphere could lead to the suppression of deep-level defects and the recombination at the heterojunction interface. Our result further indicates that the post annealing in water vapor can also passivate the grain boundaries at the interior of the CZTS films[33].

#### 4. Conclusions

In conclusion, we have used CP-AFM to study the band alignment between GBs and GIs of polycrystalline CIGS and CZTS thin films. Our results revealed that the conduction band shifts downward at GBs in CZTS, similar to CIGS; while the valence band shifts upward at GBs, in contrast to CIGS. Instead of hole deletion, hole accumulation at GBs increases carrier recombination, exacerbated by photocurrent enhancement at GBs caused by downward conduction band bending. This band

alignment is expected to be responsible partially for the low efficiency of the CZTS solar cells. Based on such understanding, oxidative annealing was deployed to engineer the band alignment in CZTS. This turns the valence band bending from upward to downward, which leads to an improvement of the local photovoltaic performance at GBs and efficiency increase of the solar cell device. Our work not only provides mechanistic understanding of the critical role of band alignment at the grain boundaries in thin film solar cells, but also points out the importance of grain boundary passivation as an effective route for enhancing their performance.

### Acknowledgement

We thank Prof. Weikun Ge for the valuable discussion and comments. The work was supported by the National Key R&D Program of China Grant nos. 2018YFB1500200, the National Natural Science Foundation of China under Grant nos. 61804159, 61674073 and 61774164, the Basic Research Program of Shenzhen (No. JCYJ20170413153246713), Science and Technology Planning Project of Guangdong Province (No.2017A050506056), Research grants of Hong Kong (GRF 14319416, 14301318 and direct grants)

- [1] F. Jiang, S. Ikeda, Z. Tang, T. Minemoto, W. Septina, T. Harada, M. Matsumura, Prog. Photovolt. Res. Appl. 23 (2015) 1884–1895.
- [2] D. Shin, B. Saparov, D.B. Mitzi, Adv. Energy Mater. 7 (2017) 1602366.
- [3] T. Kato, H. Hiroi, N. Sakai, S. Muraoka and H. Sugimoto, 27th European Photovoltaic Solar Energy Conference, 2012, DOI: 10.4229/27thEUPVSEC2012-3CO.4.2.
- [4] NREL, Best Research-Cell Efficiencies, <a href="https://www.nrel.gov/pv/assets/pdfs">https://www.nrel.gov/pv/assets/pdfs</a> /cell-pv-eff-emergingpv-rev210726.pdf(accessed:October 2022).
- [5] T.K. Todorov, J. Tang, S. Bag, O. Gunawan, T. Gokmen, Y. Zhu, D.B. Mitzi, Adv. Energy Mater. 3 (2013) 34–38.
- [6] D.A.R. Barkhouse, O. Gunawan, T. Gokmen, T.K. Todorov, D.B. Mitzi. Prog, Photovoltaics 20 (2012) 6-11.
- [7] J. J. Scragg, P. J. Dale, D. Colombara, L. M. Peter. ChemPhysChem, 13 (2012) 3035.
- [8] B. Shin, O. Gunawan, Y. Zhu, N. A. Bojarczuk, S. J. Chey, S. Guha. Prog. Photovoltaics, 9 (2013) 72.
- [9] S. Siebentritt, S. Schorr, Prog. Photovolt. Res. Appl. 20 (2012) 512–519.
- [10] J.B. Li, V. Chawla, B.M. Clemens, Adv. Mater. 24 (2012) 720–723.
- [11] P. Jackson, R. Wuerz, D.Hariskos, E. Lotter, W. Witte, M. Powalla, Phys. Status Solidi RRL 10 (2016) 583–586.
- [12] T. Gershon, B. Shin, N. Bojarczuk, T. Gokmen, S. Lu, S. Guha, J. Appl. Phys. 114 (2013) 154905.
- [13] W.K. Metzger, I.L. Repins, M.A. Contreras, Appl. Phys. Lett. 93 (2008) 022110.
- [14] S. Chen, J.H. Yang, X.G. Gong, A. Walsh, S.H. Wei, Phys. Rev. B. 81 (2010) 245204.
- [15] S. Chen, A. Walsh, X. G. Gong, S.H. Wei, Adv. Mater. 25 (2013) 1522.
- [16] S. Chen, X. Gong, A. Walsh, S.H. Wei, Appl. Phys. Lett. 96 (2010) 021902.
- [17] A. Wang, M. He, M. A. Green, K. Sun, and X. Hao, Adv. Ener. Mater. 13 (2022) 2203046.
- [18] C. Li, Y. Wu, J. Poplawsky, T. J. Pennycook, N. Paudel, W. Yin, S. J. Haigh, M. P. Oxley, A.
- R. Lupini, M. Al-Jassim, S. J. Pennycook, and Y. Yan, Phys. Rev. Lett. 112, (2014) 156103.
- [19] Y. Lei, Y. Li and Z. Jin, Energy Reviews, 1 (2022), 100003.
- [20] C. Persson, A. Zunger, Phys. Rev. Lett. 91 (2003) 266401.
- [21] C.S. Jiang, R. Noufi, K. Ramanathan, J. A. AbuShama, H. R. Moutinho, M. M. Al-Jassim,

- Appl. Phys. Lett. 84 (2004) 3477-3479.
- [22] M. Takihara, T. Minemoto, Y. Wakisaka, and T. Takahashi, In:Proceedings of the 35th IEEE Photovoltaic Specialists Conference, (2010), 002512-002515.
- [23] W. Li, Y. Ma, S. Yang, J. Gong, S. Zhang, X. Xiao, Nano Energy 33 (2017) 157-167.
- [24] D. Azulay, O. Millo, I. Balberg, H.-W. Schock, I.Visoly-Fisher, D. Cahen, Sol. Energy Mater. Sol. Cells 91 (2007) 85-90.
- [25] A. Polizzotti, I.L. Repins, R. Noufi, S.H. Wei, D.B. Mitzic, Energy Environ. Sci. 6 (2013) 3171–3182.
- [26] K. Wang, B. Shin, K.B. Reuter, T. Todorov, D.B. Mitzi, S. Guha, Appl. Phys. Lett. 98 (2011) 051912.
- [27] J. Li, D.B. Mitzi, V.B. Shenoy, ACS Nano 5 (2011) 8613-8619.
- [28] W.J. Yin, Y. Wu, S.H. Wei, R. Noufi, M.M. Al-Jassim, Y. Yan, Adv. Energy Mater. 4 (2014) 1300712.
- [29] M. Wong, K. Tse, and J. Zhu, J. Phys. Chem. C, 122 (2018), 7759–7770
- [30] K. Zhang, C. Yang a L.Yin, Z. Liu, Q. Song, X. Xiao, Sol. Energy Mater. Sol. Cells.,120 (2013) 253–258.
- [31] Y. Feng, Y. Fan, Q. Song, Z. Li, W. Li, J. Tong, C. Yang, Sur. & Coat. Tech., 320(2017) 65–69
- [32] W. Li, S. R. Cohen, D. Cahen, Sol. Energy Mater. Sol. Cells., 120 (2014) 500-504
- [33] H. Sun, . Huang, T. L. Young, J. Cong, J. Li, K. Sun, C. Yan, A. M. Soufiani, X. Cui, M. P. Nielsen, X. Zhang, J. A. Stride, M. A. Green, and X. Hao, Adv. Optical Mater., 10, (2022), 2200607

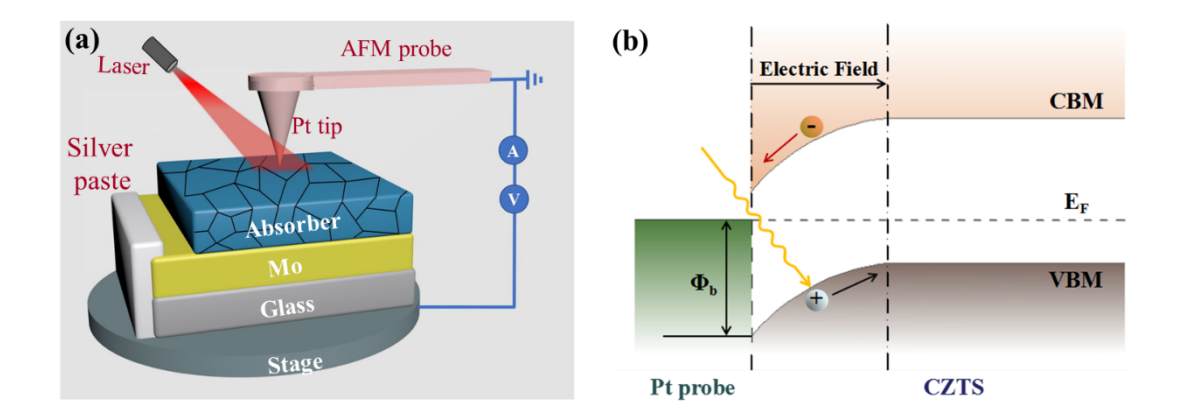


**Figure 1**. (a) A schematic diagram of the experimental setup for CP-AFM used to study the CIGS and CZTS absorber thin films, (b) a schematic band diagram to illustrate the Schottky barrier and built-in electric field formed across the Pt/semiconductor junction. Upon light illumination, the AFM tip serves as an electrode to probe the microscopic electronic structure and carrier transport at the nanoscale resolution.

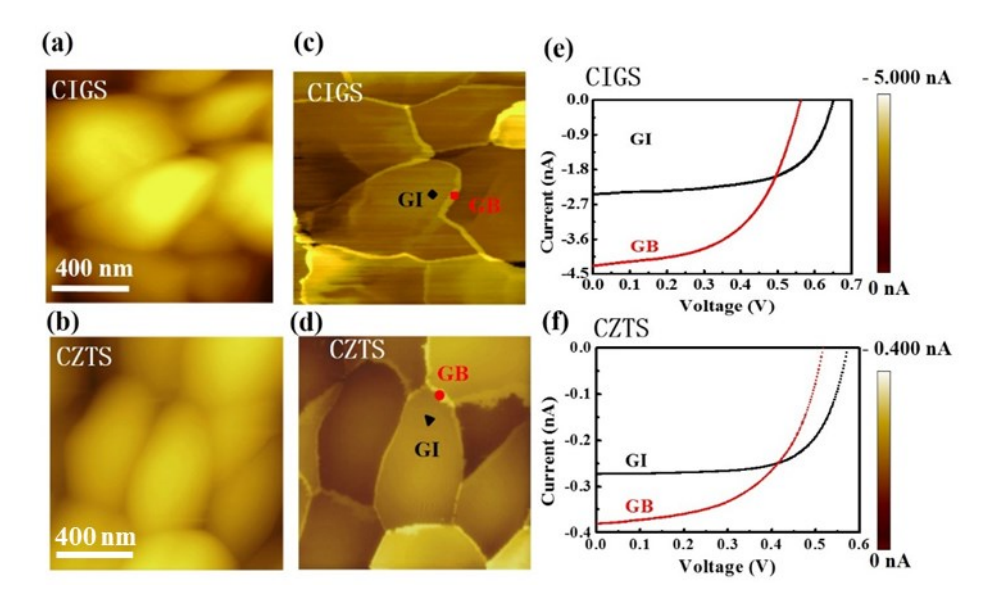


**Figure 2**. (a) and (b) are the measured morphology of CIGS and CZTS thin films, respectively. (c) and (d) are the photocurrent mapping for CIGS and CZTS, respectively. The bright contrast at GBs suggest that the photocurrent are enhanced at GBs for both CIGS and CZTS, indicating electron accumulation at GBs. (e) and (f) present the photocurrent I-V curves measured at selected positions in current mapping for CIGS and CZTS, respectively.

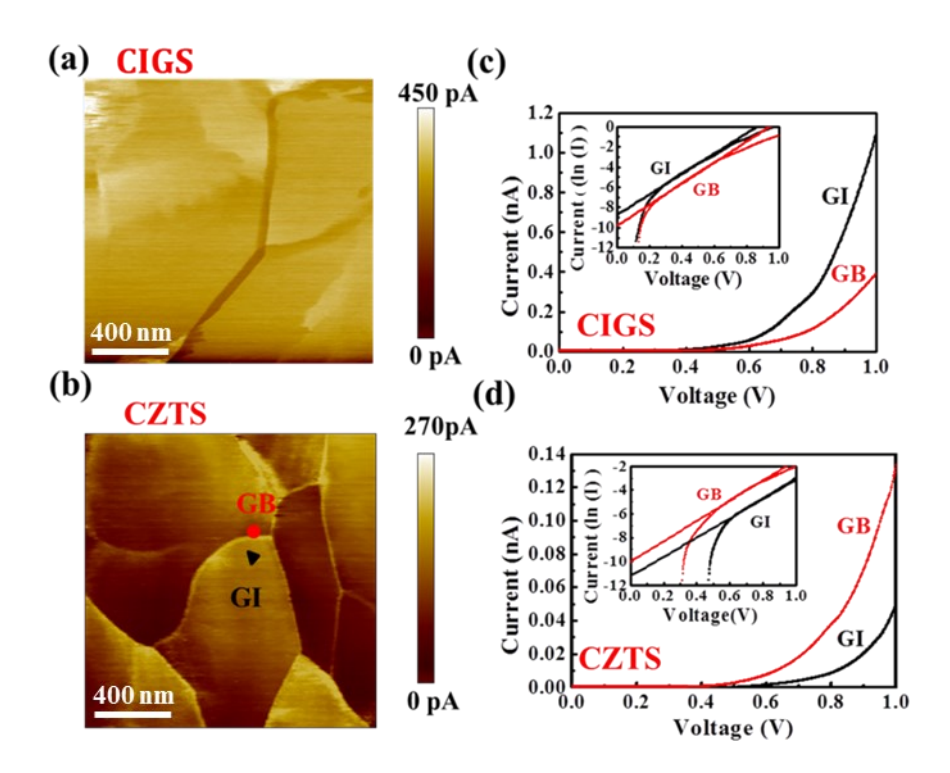


**Figure 3**. (a) and (b) are the tunneling current mapping of CIGS and CZTS, respectively. GBs show up as dark boundaries in CIGS, while bright lines are found in CZTS. Tunneling I-V curves measured at selected positions around GBs are shown for (c) CIGS and (d) CZTS, respectively. The I-V curves clearly demonstrate that the tunneling current is smaller at GBs for CIGS, while it is larger at GBs for CZTS.

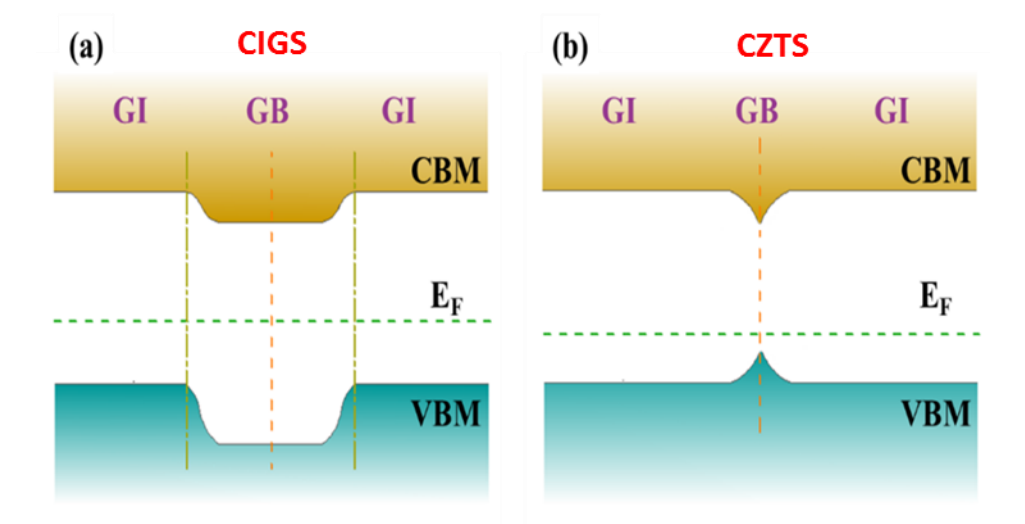


**Figure 4**. The proposed band alignment diagrams between the GIs and GBs in CIGS and CZTS thin films. For CIGS, the downward bending for both conduction band and valance band forms a type-II band alignment which enhances the separating of the electron and holes. While for CZTS, the downward conduction band bending and the upward valance band bending form traps for both electrons and holes, which enhances the recombination of the electrons and holes. From AFM observations, GBs are noticeably narrower in CZTS.

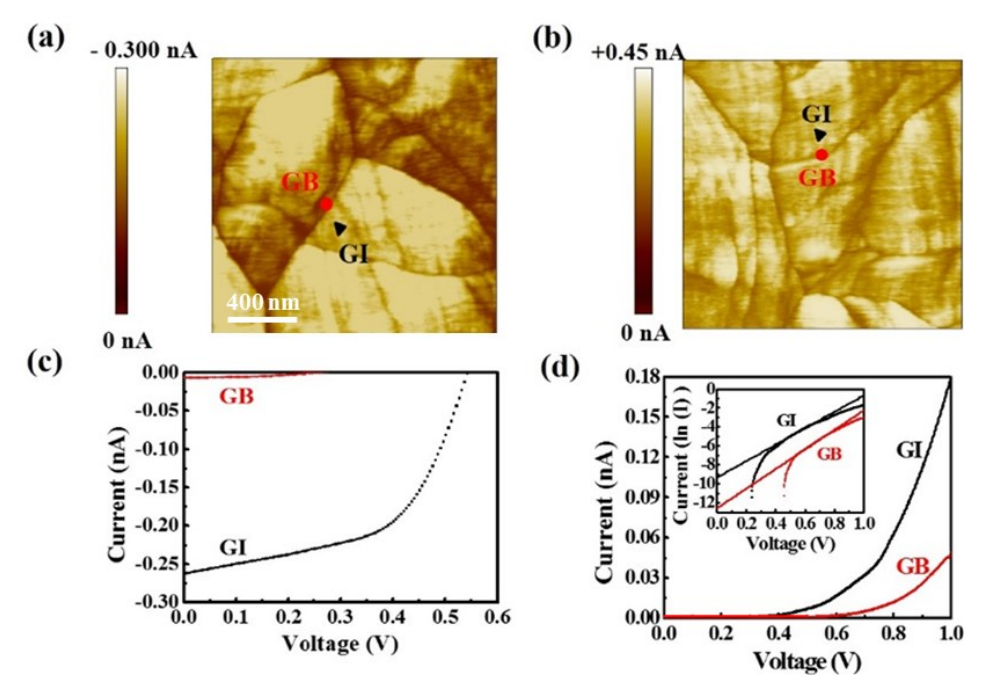


**Figure 5**. (a) Photocurrent and (b) tunneling current mapping of CZTS after air annealing. Dark GBs are observed in both images, indicating that carriers are blocked outside the GBs in the CZTS film after air annealing. (c) The photocurrent I-V curves measured at selected positions marked as GB and GI as shown in (a). The photocurrent at GB is an order of magnitude lower than that at GI. (d) gives the tunneling I-V curves at GB and GI as indicated in (b). The inset in (d) shows the I-V curves in semi-logarithmic scale together with linear fittings to extrapolate the Schottky barrier height. The air annealing treatment modifies the electronic structure of the GBs in CZTS significantly.

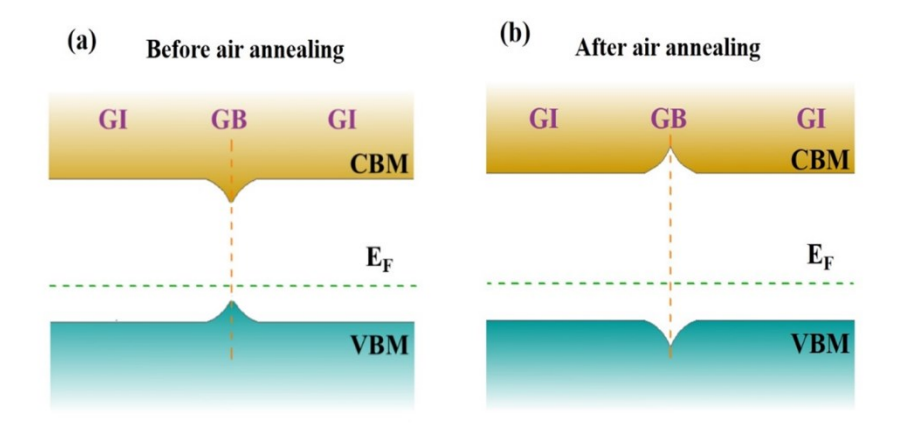


**Figure 6**. The proposed band alignment diagrams of CZTS around GBs (a) before and (b) after air annealing.

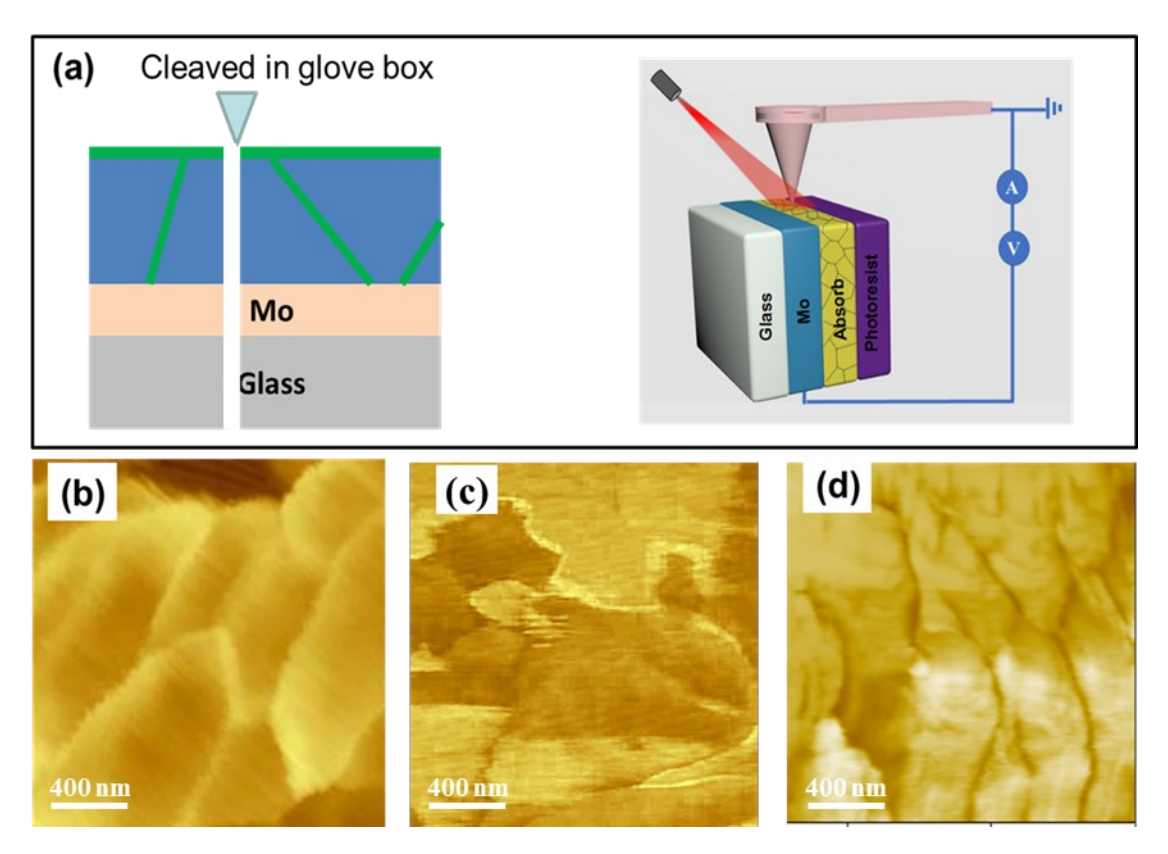


**Figure 7**. (a) schematic diagram of the cross-section C-AFM measurement. The sample is cleaved in glove box to get fresh surfaces. (b), (c) and (d) are the cross-section tunneling current mapping of the CZTS thin films for untreated, treated using dry air and treated using nitrogen with saturated water vapor.